Using Computer Microvision to Characterize the Motions of a Microfabricated Gyroscope

by

Laura Karine Johnson

Submitted to the Department of Electrical Engineering and Computer Science
in partial fulfillment of the requirements for the degree of

Master of Science in Electrical Engineering and Computer Science

at the

MASSACHUSETTS INSTITUTE OF TECHNOLOGY

June 1997

Author ....
Department of Electrical Engineering and Computer Science
May 23, 1997

Certified by .....
Dennis M. Freeman
Assistant Professor of Electrical Engineering
Thesis Supervisor

Certified by .....
C. Quentin Davis
Ph.D. Candidate in Electrical Engineering
Associate Supervisor

Accepted by .....
Arthur C. Smith
Chair, Departmental Committee on Graduate Students

Using Computer Microvision to Characterize the Motions of a Microfabricated Gyroscope

by

Laura Karine Johnson

Submitted to the Department of Electrical Engineering and Computer Science
on May 23, 1997, in partial fulfillment of the
requirements for the degree of
Master of Science in Electrical Engineering and Computer Science

Abstract

The commercial importance of microfabricated sensors is increasing rapidly. However, tools for design and characterization of microelectromechanical systems (MEMS) remain primitive in comparison to those for their electronic counterparts. In response, we have developed a method to characterize the motions of MEMS. Our method, called computer microvision, combines video microscopy and computer vision to estimate 3-D motions with nanometer precision. To test computer microvision, a microfabricated gyroscope from the Charles Stark Draper Laboratory was studied. The gyroscope is an angular rate sensor whose area is less than 1 square mm. It consists of two masses driven to vibrate at a high frequency (20 kHz) in the plane of the structure. Rotations of the gyroscope induce out-of-plane motions of the masses which are proportional to the angular velocity of the gyroscope.

The structure of the gyroscope make it a difficult target of study. The masses have periodically spaced holes through which the substrate is visible. To unambiguously meaure motions of the masses, small regions between adjacent perforations were analyzed. Reliability is assessed by comparing results from different regions. Initial results reveal problems with the original system. These problems are described, along with the improvements that lead to more accurate and robust performance.

The improved system is applied to measure both in-plane and out-of-plane motions of the gyroscope. A 3-D frequency response of the gyroscope demonstrating both in-plane and out-of-plane resonances is described. In addition, out-of-plane levitation and rocking modes of motion are analyzed, and a frequency responses of these modes are shown. The out-of-plane motions are of particular interest because they affect the sensitivity of the gyroscope.

Thesis Supervisor: Dennis M. Freeman
Title: Assistant Professor of Electrical Engineering

Associate Supervisor: C. Quentin Davis
Title: Ph.D. Candidate in Electrical Engineering

Acknowledgments

First, I would like to thank my advisors, Denny Freeman and Quentin Davis. Denny taught me how to give presentations, improved my writing, and helped solve all my problems when I was sure I would never find a solution. I would like to Thank him for always reassuring me I was doing fine and taking time to explain things when I didn't understand them. Quentin has spent countless hours answering questions, fixing problems, and giving me suggestions. I would like to thank him for always helping me with a smile and for giving me a taste of what it's like to have a big brother by beating on me all the time.

I would also like to thank all of the micromechanics lab group for all their help and for making the 8th floor a fun place to work. Thanks Zoher Karu, for getting me started; Cameron Abnet, for morning conversations and commiseration; AJ Aranyosi, for always being willing to lend a helping hand; Anthony Patire, for not taking MIT too seriously and teaching me to dance; Rosanne Rouf, for helping me keep my sanity in this crazy place; and Michael Mermelstein, for his interesting perspectives. Special thanks to Denny, Quentin, AJ, and Cam for proofreading and improving my thesis.

I would like to thank all my friends, especially all the 4th floor residents at Ashdown, who made MIT a fun and interesting place in spite of the stress. Most especially, I want to thank Juan Bruno, who made sure I had a decent meal every night, ran errands and did chores for me when I was stressed, and gave much needed moral support. I couldn't have finished without your help.

Lastly, I want to thank my family. I wouldn't be here without you. I especially want to thank my parents, Marilyn and Walt Johnson, for all their love and support. Thanks Dad, for encouraging me to go into engineering, and Mom, for daily e-mails that kept me connected with the outside world. I also want to thank my sisters, Krista, Shireen, Jannika, and Emily, for being my best friends, making me laugh, and being there when I needed someone to talk to. You guys are great!

Contents

Chapter 1

Introduction

In little more than a decade, microelectromechanical systems (MEMS) have grown from scientific curiosities to commercial products (O'Connor, 1992). VLSI techniques similar to those used to fabricate electronic chips are used to combine mechanical and electronic components on a single chip to make miniature structures such as sensors, actuators, and valves. However, unlike electronic chips, these microelectromechanical devices lack extensive tools for testing and characterizing failure modes (Freeman and Davis, 1996). This lack of tools makes design, development, and testing of MEMS a slow process. To address this issue, our group has developed a system that holds potential to contribute to the development of MEMS by providing a tool for test and verification. We call the system computer microvision.

Computer microvision combines video light microscopy, stroboscopic illumination, and machine vision to measure three-dimensional motions of microscopic structures (Davis, 1994). The microscope projects magnified images of a micromachine onto a scientific grade CCD camera. The micromachine is excited with a periodic stimulus, and stroboscopic illumination is used to take stop-action images of the resulting motion. Stop-action images are recorded at multiple planes of focus to form a time sequence of 3-D images. The recorded images can be viewed at playback speeds to facilitate human interpretation of the three-dimensional motions. The images can also be analyzed using computer vision algorithms to give quantitative estimates of the motion of any structure in the images.

Computer microvision was developed to measure motions of biological structures (Davis, 1994). It was later applied to a microfabricated accelerometer, demonstrating its potential as a measurement tool for MEMS (Freeman and Davis, 1996). This project further investigates the usefulness of computer microvision as a tool for characterizing MEMS devices. The focus of the investigation is a microfabricated gyroscope (Bernstein et al., 1993) from the Charles Stark Draper Laboratory (Cambridge, MA).

The gyroscope is a useful test structure because its operation is intrinsically three-dimensional. The gyroscope consists of two masses (shuttles) suspended above the substrate via a folded-beam cantilever spring system (Figure 1-1). The shuttles are driven by electrostatic forces applied through comb drives so that they oscillate at a high frequency in the plane of the structure (Weinberg et al., 1994). Rotation of the gyroscope induces motions of the shuttles that are perpendicular to the plane of the substrate (Figure 1-2). These out-of-plane motions are a direct consequence of the principle of inertia. The shuttles are driven to move parallel to the substrate. Rotations of the substrate cause forces in the springs that act to change the direction of motion of the shuttles. However, inertia prevents the shuttles from changing their direction instantaneously. Consequently, angular velocities of the gyroscope cause the shuttles to change their elevation above the substrate.

Although the source of out-of-plane motions is easy to understand from an inertial reference frame, we sometimes view the shuttle from a frame of reference attached to the substrate, which is the important frame of reference for the sense electronics. In that frame of reference, the out-of-plane motions seem mysterious because they are being viewed from a non-inertial reference frame. In the non-inertial reference frame, it is convenient to think about the out-of-plane motions in terms of a fictitious force, the Coriolis force. The Coriolis force is due to the shuttles having velocities relative to a rotating reference — the substrate of the gyroscope. The Coriolis force on each shuttle is

$$F = -2m\Omega v \tag{1.1}$$

where m is the mass of the gyroscope shuttle, Ω is the angular velocity of the substrate,

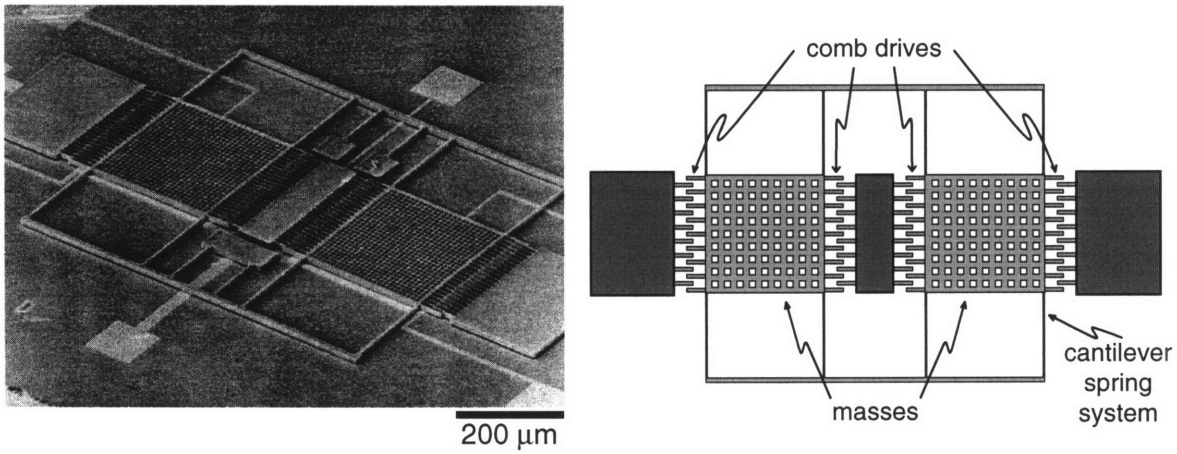

Figure 1-1: Microfabricated gyroscope. The image (left) shows a scanning electron micrograph of a gyroscope (courtesy of Mark Weinberg, (Weinberg et al., 1994)). The schematic (right) shows the two shuttles, which are suspended above the substrate by a system of cantilever springs. The dark boxes are fixed to the substrate, and the fixed teeth of the comb drives are attached to them. The thin beams of the cantilever spring system flex so that the shuttles move back and forth when a force is exerted on them from the comb drives.

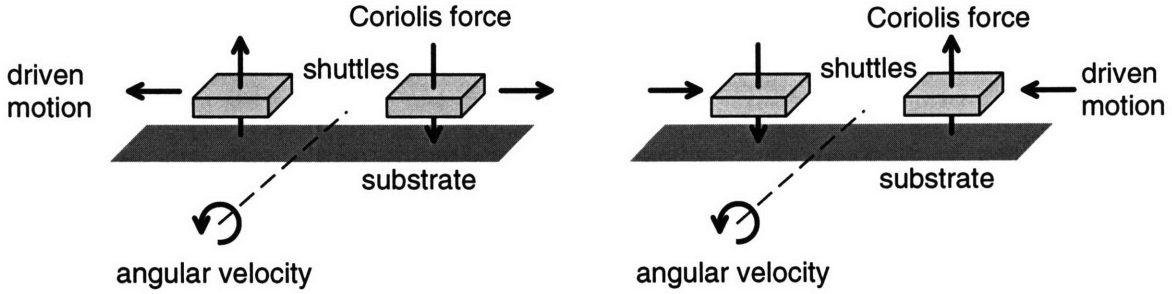

Figure 1-2: Gyroscope motions. Two shuttles (supported by springs, not shown) are driven to oscillate parallel to the substrate. Rotation of the substrate induces Coriolis forces that move the shuttles orthogonal to the driven motion. The magnitude of the orthogonal displacement is proportional to the angular velocity of the substrate.

and v is the velocity of the shuttle. (Section 8.5, Kleppner and Kolenkow, 1973). As can be seen in Eq. 1.1, the Coriolis force is proportional to the angular velocity of the gyroscope. Because the impedance to out-of-plane motions is spring-like, the out-of-plane displacement is also directly proportional to angular velocity. The changing distance between the shuttles and the substrate can be measured as a change in capacitance between each shuttle and the substrate. The difference between the two capacitances is used to calculate the angular velocity of the gyroscope. Thus the gyroscope acts as an angular velocity sensor.

The sensitivity of the gyroscope depends on accurate measurement of the out-of-plane motions induced by the Coriolis force. However, other mechanisms such as mechanical and electrical asymmetries can also cause out-of-plane motions. These unintended out-of-plane motions can be misinterpreted as angular velocities, thus limiting the sensitivity of the gyroscope. The focus of my project is to use computer microvision to measure motions of the gyroscope, particularly unintended out-of-plane motions that are present when the gyroscope is not rotating. Determining what unintended out-of-plane motions exist is the first step in understanding the mechanisms responsible for these errors so that future designs can be improved.

My investigation of the gyroscope is also an important test of the computer microvision system. Unlike the biological structures for which computer microvision was developed, we have considerable a priori knowledge of how the gyroscope should behave. For example, we expect rigid body motion of the gyroscope shuttles. Therefore, if the motion estimated by the system is not consistent with this assumption, we assume there is a problem with the measurement system and not with the gyroscope. The degree of consistency among motion estimates for the gyroscope gives us a measure of the accuracy and robustness of the system. By using computer microvision to analyze the gyroscope, we can assess the generality with which computer microvision can be applied as an analysis tool for MEMS.

Chapter 2

Methods

The gyroscope is intended to be operated in a vacuum and controlled by custom built-in electronics. However, in this study we operated the gyroscope in air at atmospheric pressure and controlled the gyroscope with voltage waveforms generated under computer control. Analysis using computer microvision can be broken into two steps: data acquisition and data analysis. Data acquisition involves collecting images of the gyroscope using video microscopy; the analysis uses computer vision algorithms to estimate motions from the images. The process is discussed in the following sections.

2.1 Data Acquisition

2.1.1 Gyroscope Setup

Each gyroscope chip is mounted on a glass slide using wax to hold it in place. The gyroscope is placed on the stage of a light microscope (Zeiss Axioplan, Thornwood, NY), with a customized stage that is large enough to hold micromanipulators. The gyroscope is excited using an electrical stimulus delivered via small probes (Rucker & Kolls, Inc., Mipitas, CA, #25935-001 and #25935-002) held in place with the micromanipulators (Rucker & Kolls, Inc., Mipitas, CA, #25935-001 and #25935-002). The probes are bent to an angle of 15 degrees between the probe and the stage

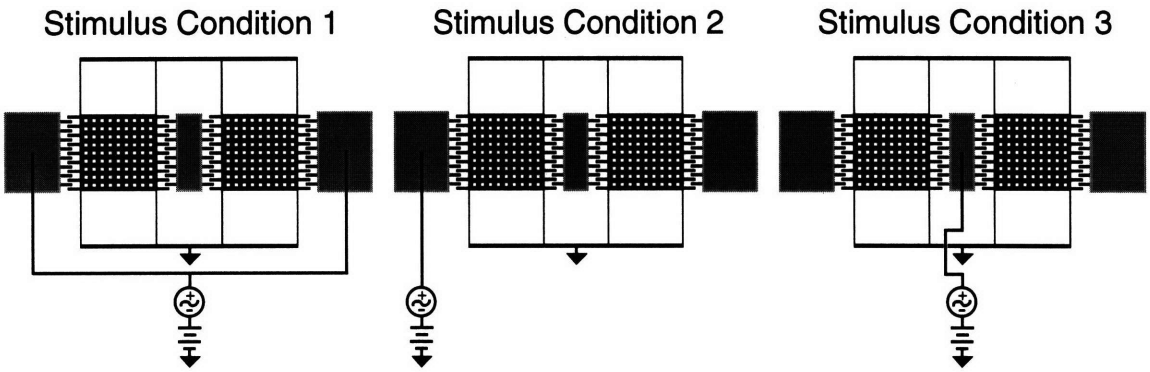

Figure 2-1: Stimulus conditions used in analyzing the gyroscope. The first condition used three probes; the other two use two. In condition one, the signal is applied to each of the outer combs of the gyroscope. In condition two, only one side of the gyroscope is stimulated. In condition three, the inner comb of one shuttle is stimulated. In all three cases, the shuttles are grounded.

so that the probes would fit under the objective and not interfere with the light path.

The typical stimulus configuration uses three probes. Two probes drive the outer combs using a sinusoidal signal plus a DC offset (typically 40 V AC peak-to-peak + 20 V DC). Another probe grounds the shuttles. This configuration is illustrated in Figure 2-1 as stimulus condition 1. This stimulus condition induces a "tuning fork" mode of motion in which the shuttles move back and forth in opposite directions, like the tines of a tuning fork. This is the desired mode of motion for operation as a gyroscope. Other modes of motion can be excited using different stimulus conditions. A two-probe stimulus condition was analyzed where one probe was used to excite the outside comb of one shuttle, and the other probe grounded the shuttles (Figure 2-1, stimulus condition 2). Under this stimulus condition, two modes of motion were observed. The tuning fork mode could still be excited, and a second "hula" mode in which the shuttles moved back and forth in the same direction was also excited. A third stimulus condition was analyzed in which an inner comb of one shuttle was excited and the shuttles were grounded (Figure 2-1, stimulus condition 3). This stimulus condition accentuated a complex out-of-plane mode of motion which will be discussed later.

2.1.2 Video Microscopy

The gyroscope is magnified using epi-illuminated brightfield microscopy. The moving gyroscope is imaged using a scientific grade CCD camera (Photometrics 200 series, 12 bit dynamic range, Photometrics, AZ). The stage on which the gyroscope is mounted is computer-controlled, and can be moved vertically in increments of $1/11$ μm. Optical sectioning (Inoué, 1986; Freeman and Davis, 1996) is used to obtain images of the gyroscope at a series of planes of focus. Three objectives are used for data acquisition: a 40× 0.5 NA objective, (Nikon M Plan 40, #322791, 5 mm working distance, Japan) a 20× 0.4 NA objective (Zeiss LD-Epiplan, #442840, 9.8 mm working distance), and a 50× 0.6 NA objective (Zeiss LD-Epiplan, #442851, 3.5 mm working distance). A vibration isolation table is used to reduce mechanical vibrations, which can affect motion estimates.

2.1.3 Stroboscopic Illumination

Stroboscopic illumination is used to take images at evenly spaced phases (typically 8) of the stimulus frequency. The light source used is either a gas-discharge strobe light (model #8440, Chadwick-Helmuth, CA) plus a fiber optic scrambler (Technical Video, Ltd., Woods Hole, MA), or an LED (1 candela diffused red LED with 60° viewing angle, #CMD53SRD/G, Chicago Miniature Lamp, Buffalo Grove, IL. or 4.1 candela non-diffused red LED with 8° viewing angle, #AND180CRP, AND division of Purdy Electronics, CA). The strobe pulse varies in length and duration and has a pulse width of approximately 12 μs, which limits the range of stimulating frequencies. The LED is generally superior because the light level is both spatially and temporally uniform and can be more precisely controlled. The LED can also be used to sample at a much faster rate. However, the strobe is orders of magnitude brighter than the LED, which does not always provide enough light. The results presented in Chapter 4 were obtained using the strobe because it was part of the original system; however, we found the LED to be generally superior, and all other results were obtained using the LED.

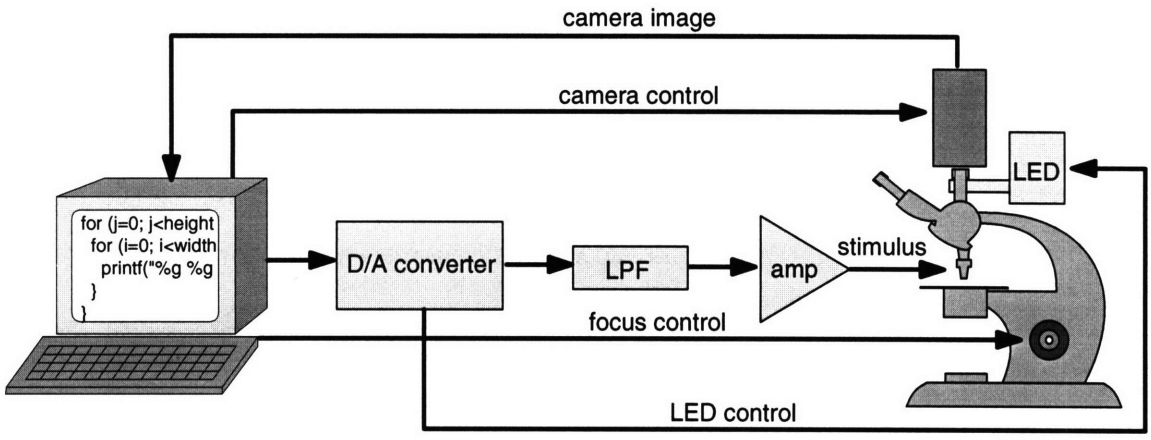

Figure 2-2: Experimental apparatus. The experiment is run by the computer, which controls a D/A converter and the camera for image acquisition. The D/A converter produces a stimulus signal for the gyroscope and a control signal for the LED. The stimulus is filtered and amplified before it reaches the gyroscope. The camera writes the images back to the computer.

2.1.4 Real-Time I/O System

Data acquisition is completely automated. The computer sends a signal to the camera to begin image acquisition. It also controls a D/A converter (12 bit, DT 1497, Data Translations) which generates the sinusoidal stimulus used to excite the gyroscope, as well as the control signal for the strobe. The control signal to the strobe is synchronized with the desired phase of the stimulus. The stimulus waveform is passed through a low-pass filter (11 pole elliptical, TTE, CA, cut-off at 22 kHz or 6 pole Chebyshev, Type I, 0.5 dB ripple, cut-off at 48 kHz (pp. 274-275, Horowitz and Hill, 1991)), and then amplified using a 40 dB power amplifier. The amplified stimulus signal drives the gyroscope. The camera writes the images back to the computer (Figure 2-2).

As shown in Figure 2-3, the amplitude of the stimulus is ramped up using a Hanning window. Once the stimulus is at full amplitude, the LED is strobed at the appropriate phase of the stimulus. Then the signal ramps down. This process is repeated until sufficient light has been collected. The image is then read from the camera, and the process is repeated to obtain an image for the next stimulus phase.

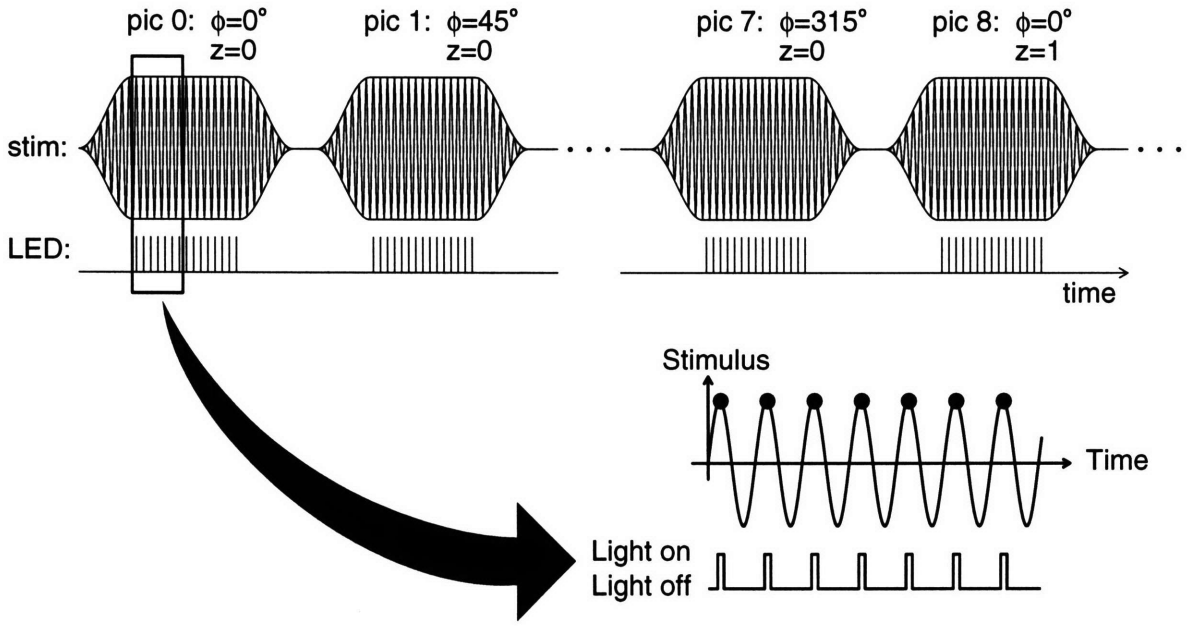

Figure 2-3: LED and stimulus signals. The top drawing shows the stimulus and LED signals used to obtain each image. Eight images are taken for evenly-spaced phases (ϕ) of the stimulus, at which point the stage moves (z position changes from 0 to 1), and the process starts again. The bottom drawing shows an expanded version of the stimulus and LED signals, demonstrating how the light is turned on and off to image the gyroscope during one phase of the stimulus. A different phase is used for the next image.

2.1.5 Experimental Protocol

Imaging starts by focusing below the plane at which the gyroscope is in sharpest focus. Images are taken for 8 evenly-spaced phases of the stimulus. The stage then moves so that images can be taken at a higher focal plane. A 20 second settling time is allowed before starting to take the subsequent data. Typically, 30 planes of focus are taken, each separated by 6/11 μm. The gyroscope is in sharpest focus at the middle planes. The resulting data forms a volume for each phase of the stimulus, giving a 3-D image for each phase. These images can be analyzed to obtain three-dimensional estimates of the motion.

2.2 Data Analysis

2.2.1 Two Point Correction

The first step in analyzing the images is correcting for fixed-pattern noise. Fixed-pattern is caused by factors such as dirt on the optics, camera defects, variations in the illumination pattern, and vignetting due to optics. These factors degrade the images because they are stationary, which results in underestimation of the motion. A two-point, flat-fielding technique is used to reduce fixed pattern noise (Hiraoka et al., 1987). A dark image is formed by taking several images (typically 40) in the absence of light and averaging them together. To form a background image, a front surface mirror is used to reflect the light and give a uniform background. Alternatively, a background image can be formed by taking images at a plane well above the plane where the gyroscope is in focus, so the gyroscope is no longer visible. Again, 40 images are averaged to obtain the background image. The dark image E_d is subtracted from the raw image E_r and from the background image E_b to remove offset in the images. The images are then divided on a pixel-by-pixel basis to yield a corrected image, E_c:

$$E_c[i,j] = \frac{E_r[i,j] - E_d[i,j]}{E_b[i,j] - E_d[i,j]} \tag{2.1}$$

This technique typically reduces the energy in the fixed pattern noise by a factor of three (Davis and Freeman, 1997), while increasing the shot noise in the corrected image over that in the original image by only about 1% (Aranyosi, 1997).

2.2.2 Motion Detection Algorithm

We use a gradient method (Horn and Schunck, 1981; Horn and Weldon, Jr., 1988) to estimate motions from changes in brightness. Gradient methods can detect motions that are smaller than a pixel, as shown in Figure 2-4. Even though the gradient method is among the best in the literature, motion estimates based on gradients are statistically biased. To compensate for this bias, we use a linear bias compensation scheme (Davis, 1997). The algorithm determines the best estimate of 3-D rigid body translation in a least-squares sense. We use the algorithm to estimate the displacement between successive images. Successive estimates are used to construct a displacement waveform as a function of time for one period of the stimulus. To do three-dimensional analysis, a series of two-dimensional images taken at evenly-spaced planes of focus is used to create the three-dimensional image for each time step. The algorithm then analyzes changes in gray values for all three dimensions and gives motion estimates in three directions. The time waveforms are then transformed to the Fourier domain to find the magnitude and phase or real and imaginary components of the motion. To get the phase referenced to the phase of the stimulus, phase lag due to the low-pass filter is subtracted out.

2.2.3 Analysis Region

The motion detection algorithm estimates 3-D rigid translations of a target. To apply the algorithm to targets with multiple moving parts, we must segment the image into regions that isolate parts of the image that can be approximated by rigid body motion. The selection of the region is important because the motion detection algorithm finds the best displacement in a least-squares sense of all the pixels in the region. Thus, if there were two opposing motions of equal magnitude in the region, the algorithm

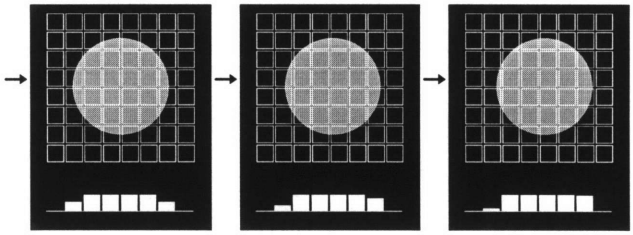

Figure 2-4: Variations in brightness caused by subpixel motions. The array of squares in each panel represents the pixels of a video camera; the gray disk represents the image of a simple scene; and the bar plots represent the brightness measured by the row of pixels indicated by the arrow. The three panels illustrate rightward motion of the disk. Although the displacements are subpixel, information about the motion is available from changes in the brightness of the pixels near the edges. Figure courtesy of Dennis Freeman (Freeman and Davis, 1996).

would give an estimate of zero motion for the region. The amount of contrast in the region and the number of pixels in the region are other factors that affect the accuracy of the estimate obtained. High contrast regions are easier to track because they have steeper intensity gradients in space and time. Larger regions mean there are more pixels to average, which will give a better estimate provided that all the pixels in the region are moving in the same direction and by the same amount. The regions we use are rectangular. For three-dimensional data sets, the regions are rectangular volumes.

2.2.4 Modeling Rigid-Body Motion

Because silicon is an extremely stiff material, the gyroscope's shuttle is well-approximated as a rigid body. For any two observation points A and B, we can denote the out-of-plane displacement waveform seen at the points as $d(A,t)$ and $d(B,t)$. The rigid body motion assumption means that the shuttle will always be a straight line at any point in time. Since two points determine a line, the motion at any position along the shuttle can be defined in terms of the motion of the two known points

$$d(x,t) = \frac{x-B}{A-B}d_A(t) + \frac{x-A}{B-A}d_B(t) \equiv d_C(t) + xd_D(t) \tag{2.2}$$

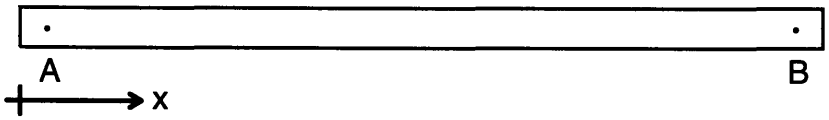

Figure 2-5: Model of the shuttle. The rectangle represents the shuttle, and A and B are two known points on the shuttle. The distance from the edge of the shuttle is denoted as x.

We define all the terms that do not include x as d_C and all the terms that are multiplied by x as d_D, which demonstrates that the out-of-plane position of the points along the shuttle is linear at any given time. The spatial position of the points is also linear at any frequency, as can be seen by taking the Fourier Transform of the time waveforms

$$D = \mathcal{F}\{\mathrm{d}\} \tag{2.3}$$

$$D(x, \omega) = D_C(\omega) + xD_D(\omega) \tag{2.4}$$

From this equation it is clear that the real and imaginary components of the motion will also fall on straight lines. This fact is used in Chapter 3 to test the consistency of results obtained using computer microvision.

Chapter 3

Improvements to Computer Microvision

In order for computer microvision to become a useful engineering tool, we need to characterize the measurement errors that result. To that end, it is convenient to adopt a statistical approach. Repeated measurements will show variation, which can be characterized by computing the standard deviation of repeated measurements. However, the mean of arbitrarily many repeated trials may also be in error. We refer to the difference between a motion and the mean of arbitrarily many independent measurements as accuracy.

Measurements using computer microvision have previously been shown to be very repeatable (Freeman and Davis, 1996); the standard deviation of repeated in-plane measurements is typically less than 5 nm, and it is less than 13 nm for out-of-plane measurements. Quantifying accuracy is more difficult. Ideally, one would measure the motions of the same target using both computer microvision and an independent system with known accuracy. Alternatively, we can use computer microvision to measure motions of a number of different parts of the same structure. Combined with a priori knowledge about the structure (i.e., that the structure is rigid), the different measurements can be used to assess accuracy.

Given the dimensions of the shuttles of the gyroscope and the magnitudes of the forces that act on them, we expect that each shuttle will move as a rigid body. We

therefore use that expectation to test the accuracy of measurements using computer microvision as follows. We identify non-overlapping analysis regions that span the width of the shuttle (Figure 3-1). We use computer microvision to measure the out-of-plane motion of each region. Then we plot the out-of-plane displacement as a function of region number, which is equivalent to plotting as a function of distance along the shuttle. To the extent that the displacements are a linear function of region number, we can conclude that the measurements are consistent with our assumption of rigid motion (see Section 2.2.4). To the extent that the displacements are not a linear function of region number, we know that the measurements are not accurate.

Figure 3-2 shows the real and imaginary components of the out-of-plane displacement for the 13 regions shown in Figure 3-1. The measurements were repeated 5 times, and all 5 estimates are plotted with different symbols. We can see that the precision is very good; in general the 5 estimates for each individual region agree to within a symbol width. However, the estimates do not fit a straight line well. The root-mean-square differences between the out-of-plane motion estimates and the best-fitting lines are 387 nm for the real component of the motion and 207 nm for the imaginary component of motion. Identifying the source of these inconsistencies was a major part of the thesis project. It included both simulations and an investigation of various components of the computer microvision system. Several factors contributed to the inconsistent measurements, as presented in the next sections.

3.1 Out-of-Plane Simulation

Computer simulations proved to be an effective tool for understanding errors that result when computer microvision is used to measure 2-D motions (Davis, 1994). Therefore, we developed 3-D simulations to aid in our understanding of 3-D errors. To simulate out-of-plane motions, a gyroscope with no stimulus was imaged at 330 planes of focus using 1/11 μm steps between planes. Selected images from the volume were used to create a data set containing 8 volumes of 29 planes separated by 1 μm. The images were selected to simulate sinusoidal out-of-plane motion, as follows. Let

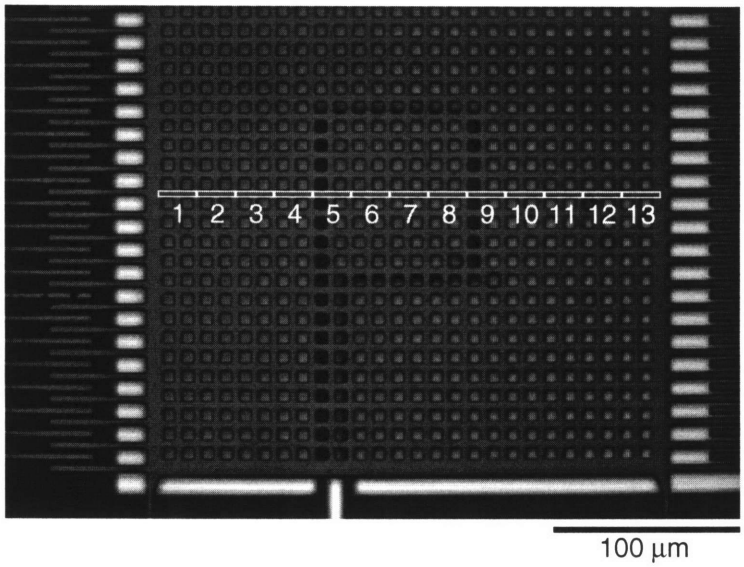

Figure 3-1: Thirteen regions across the gyroscope shuttle. These regions were analyzed to determine the motion of the shuttle.

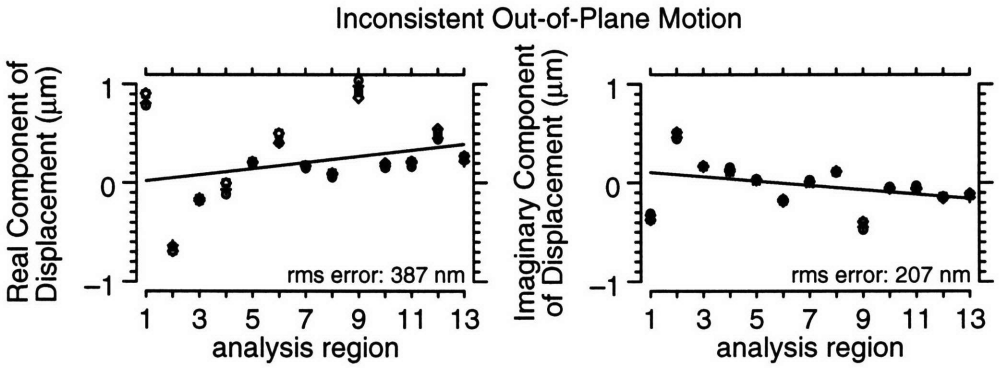

Figure 3-2: Real and imaginary components of motion for 13 regions spanning the length of the shuttle. The data were fit to lines using linear regression. Data were obtained using a 40 V peak-to-peak stimulus + 20 V DC in stimulus condition 1 (Figure 2-1 at 18.9 kHz. Thirty planes separated by 1 μm were taken at a magnification of 32×.

$P[z]$ be a plane from the original data set, where z indexes position along the optical axis ($z \in \{0, 1, .., 329\}$). Then the new data set was created using the formula $S[t, z] = P[int(11z + 3\sin\frac{\pi}{4}t)]$ where t ranged from 0 to 7 and z ranged from 1 to 29. The magnitude of the fundamental of the simulated motion was 0.530 μm peak-to-peak and the phase was 90 degrees. Thirteen regions across the shuttle were analyzed. Computer microvision estimated the motion to be 0.537 $\pm$ 0.0018 μm peak-to-peak with a phase of 90 $\pm$ 0 degrees. The results show a small amount of bias (7 nm) in the resulting estimate, and 1.8 nm of standard deviation, which is consistent with previous simulations (Davis, 1994). The measured inconsistencies in Figure 3-2 are two orders of magnitude larger than the inaccuracy suggested by the simulations. Therefore, we conclude that the simulations do not capture the physical mechanisms that most contribute to the inconsistencies in Figure 3-2.

3.2 Effect of Analysis Regions

The choice of analysis region affects the resulting motion measurement. Two effects are shown in Figure 3-3. Two of the top regions overlie a black line on the substrate. It is differentially occluded as the shuttle moves, which causes errors in motion detection. The result can be seen in Figure 3-2. Region 9 has a portion of the black line beneath it, and the estimate for region 9 does not fit well with the line. In regions that include more of the black lines, inconsistencies are even larger. The bottom regions in Figure 3-3 do not cross the black line. However, they gave even less consistent results because the stationary substrate can be seen through the holes in the shuttle.

3.3 Effect of Illumination

The illumination is a critical part of computer microvision. The motion detection algorithms are based on a constant brightness assumption, which states that the brightness of an object is independent of the location of that object. If the illumination is not consistent, then the constant brightness assumption is not met. Originally, a

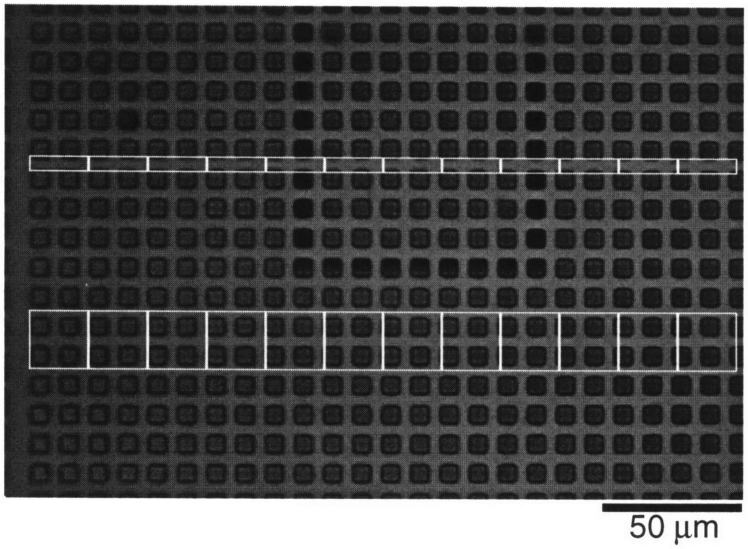

Figure 3-3: Effect of analysis regions. The bottom regions include portions of the moving shuttle and stationary substrate. The top regions include less of the substrate, but for two of the regions (5 and 9) the substrate contains dark bands.

gas-discharge strobe was used as the light source. However, the gas-discharge strobe generates pulses of light that vary in amplitude and duration. These variations limit the precision of the motion estimates. Furthermore, the long pulse width blurs the motion so that motion estimates are attenuated. Therefore we switched to LED illumination, which has little variation and can be controlled more exactly. However, the original LED (4.1 candela red LED with 8° viewing angle, #AND180CRP, AND division of Purdy Electronics, CA), which was housed in a transparent package, did not provide constant illumination at all planes of focus. A front surface mirror was used to view the illumination at each plane of focus. Figure 3-4 shows the illumination at planes 5.5 μm above and below the plane at which the mirror was in focus. An outline of the LED is clearly visible in the left image. However, the LED is not visible in the right image. Results obtained using this LED contain motion artifacts because of non-uniform illumination. A new LED (1 candela diffused red LED with 60° viewing angle, #CMD53SRD/G, Chicago Miniature Lamp, Buffalo Grove, IL) with an integrated diffuser (translucent package) was found to have more uniform illumination at all planes of focus.

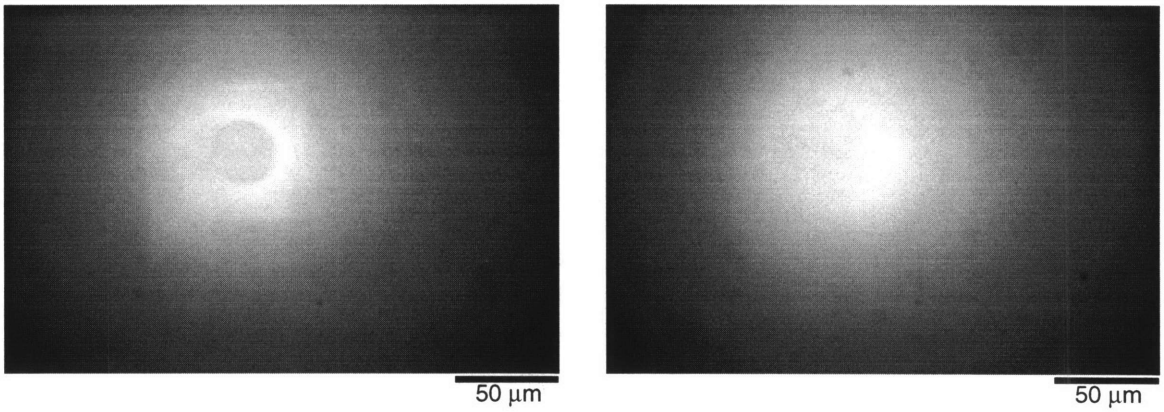

Figure 3-4: Background Images with an LED in a transparent package. The image on the left was taken 5.5 μm above the plane of focus, and the image on the right was taken 5.5 μm below the plane of focus. An image of the LED is visible in the center of the left background image, but not in the right image.

3.4 Effect of Two Point Correction

One of the largest sources of inconsistencies in the measurements was the method used to take the background images. When background images were obtained by imaging the gyroscope at a plane well above the plane of focus, spatial variations due to the gyroscope were still visible in the background image, as can be seen in the right image of Figure 3-5. This caused serious errors in the motion estimates because two-point correction introduced fixed pattern noise instead of reducing it. Using a front surface mirror creates a background image that is much more constant, as shown in the left image of Figure 3-5. Vignetting due to the LED is visible, along with dirt on the optics. This is the type of fixed pattern noise which two-point correction is intended to correct. Data were also analyzed with no two point correction to test the effectiveness of two-point correction. Two-point correction was found to decrease inconsistencies across the regions.

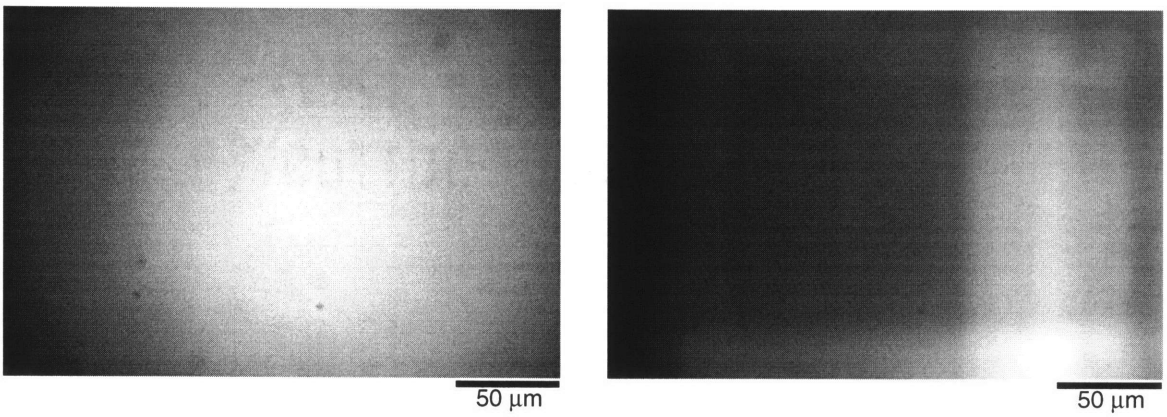

Figure 3-5: Background image acquired with a mirror (left) and with the gyroscope out-of-focus (right). An outline of the gyroscope shuttle is visible in the second image.

3.5 Magnification and Objective

The accuracy of motion estimates is affected by the magnification and numerical aperture (NA) of the objective. The results shown in Figure 3-2 were taken using a 20× objective, 0.4 NA with an optivar setting of 1.6 to give a total magnification of 32×. We would like to use a large magnification to avoid aliasing. However, we would also like to characterize modes of motion, so we would like to be able to image an entire shuttle. These two criteria are at odds with each other. The magnification of 32× causes a small amount of aliasing.

To test whether the problem was due to lower magnification causing aliasing, results from data taken with a 50×, 0.6 NA objective were compared to results taken when the magnification of the images had been effectively lowered by averaging adjacent pixels, then down-sampling by 2. This gave an effective magnification of 25×. It also reduced the number of pixels in each analysis region by a factor of 4. However, this reduction did not change the results, which implies that magnification is not the problem.

One problem with the 20× objective is its low numerical aperture (NA). A simple equation for the depth of focus of the microscope states that depth of focus is inversely proportional to numerical aperture squared (Young et al., 1993). Thus, the ratio of

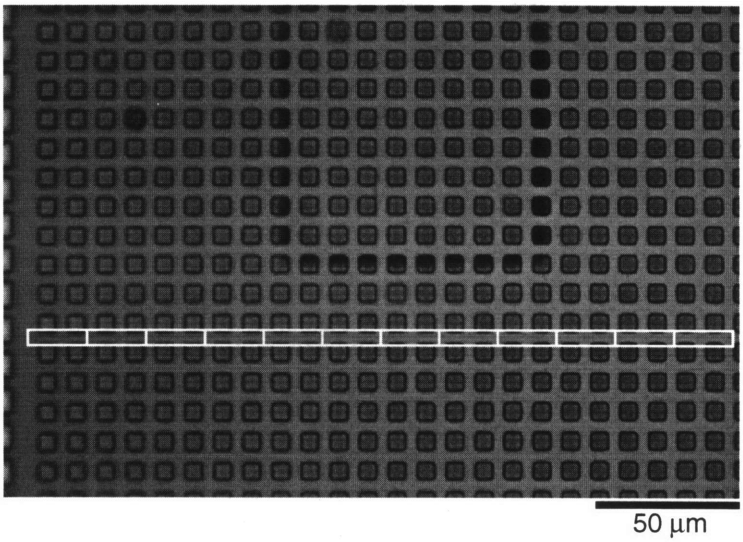

Figure 3-6: Twelve analysis regions across the shuttle. These regions were analyzed to determine the consistency of out-of-plane motions.

the depths of focus for the 20× objective with NA 0.4 to the 50× objective with NA 0.6 is 2.25. The larger depth of focus of the 20× objective blurs the image more in the out-of-plane direction, which may make the estimates less accurate.

3.6 Consistent Out-of-Plane Estimates

Data were obtained using the 50× objective, 0.6 NA and the diffused LED. Background images were taken using the front surface mirror. The data were analyzed using the regions shown in Figure 3-6. Figure 3-7 shows the real and imaginary components of the motion for each region, along with best-fitting lines. The root-mean square differences between the best-fitting line and the data are 14 nm (real component) and 9 nm (imaginary component). This error is over 25× less than the error of the estimates shown in Figure 3-2!

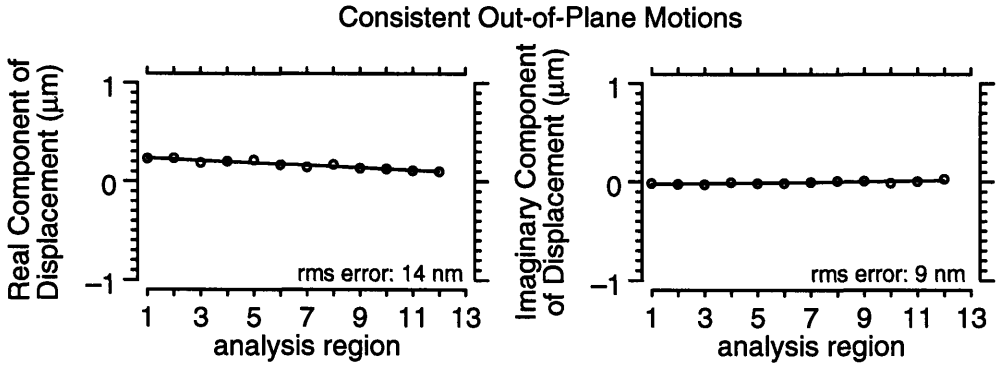

Figure 3-7: Real and imaginary components of motion for 12 regions along the shuttle. The data were taken with a 40 V peak-to-peak AC + 20 V DC stimulus at 18.9 kHz, using stimulus condition 1 (Figure 2-1). Best-fitting lines were determined using linear regression.

3.7 Relative Importance of System Improvements

To quantify the relative importance of each system improvement described above, we removed the improvements one at a time, and the root-mean-square difference between the resulting real and imaginary components of fundamental motion and the best-fitting line was computed. The square root of the squares of the real and imaginary components was then compared to 16.64 nm, which is the analogous error result for the improved system (Figure 3-7). Results are summarized in Table 3.1. The first result compares the effect of reducing the magnification by down-sampling the data to reduce the magnification by a factor of 2 as described in Section 3.5. The second shows the effect of using the regions that include the black line shown in Figure 3-3; the third shows the effect of not using two-point correction; the fourth shows the effect of the non-diffused LED; the fifth shows the problem with regions that include holes (the regions shown in Figure 3-3). The sixth result shows the difference between the 20× objective, NA 0.4 used with the optivar to give a total magnification of 32×, and the results with the 50× objective, NA 0.6 (Note that the amount of aliasing due to these two magnifications is approximately equivalent since aliasing is dependent on NA.). Note that the most significant improvement is the seventh result, the new method for obtaining background images. Using a background image

Table 3.1: Effect of Individual System Improvements on Measurement Consistency

Variation from improved system	% increase in error over rms error of 16.64 nm
reduced data set (Sec. 3.5)	5
regions with black line (Sec. 3.2)	50
no 2 point correction (Sec. 3.4)	51
non-diffused LED (Sec. 3.3)	178
regions with holes (Sec. 3.2)	179
20× objective (Sec. 3.5)	198
background image taken with gyroscope (Sec. 3.4)	708

with spatial variation due to the out-of-focus gyroscope was much worse than using no background image at all. Other improvements that greatly increased consistency include using the diffused LED, using regions which did not include the holes in the shuttle, and using the 50× objective with the higher NA.

3.7.1 Combining Effects

The errors cataloged above combine in a non-linear way. For example, using the non-diffused LED caused a 178% increase in error, using the regions with the holes caused a 179% increase in error, and not doing two point correction caused a 51% increase in error. Based on these results, one might expect using the non-diffused LED *and* using regions with holes would cause a larger increase in error than using the non-diffused LED *and* not doing two point correction. However, the former gives a 241% increase in error, and the latter gives a 397% increase in error. One might expect some problems to be coupled. For example, two-point correction is more important for the non-uniform illumination caused by the non-diffused LED than for the diffused LED, which is the LED used to characterize the effect of two-point correction in line 3 of Table 3.1.

An alternative method for comparing the importance of system improvements would be to add the results one at a time to the initial configuration (Figure 3-2). This method also demonstrates the inter-dependence of the improvements. For example,

Table 3.2: Combined Effects on Measurement Consistency

Variations from improved system	% increase in error over rms error of 16.64 nm
non-diffused LED and region with holes (Sec. 3.7.1)	241
non-diffused LED and no 2 point correction (Sec. 3.7.1)	397
20× objective, no 2 point correction, middle region used, non-diffused LED (Sec. 3.7.1)	1685
20× objective, out-of-focus background image, middle region used, non-diffused LED (Figure 3-2)	2537

the most significant source of error according to Table 3.1 is using the out-of-focus method to obtain the background images. Data obtained using this method was 7 times more inconsistent than data obtained with the improved system. At the same time, not using two point correction is one of the less significant sources of error. Thus, one might expect that the inconsistent data could be significantly improved by simply not using two point correction. However, analyzing the inconsistent data without two point correction gave a 1685% increase in error. This is a decrease in the amount of error in Figure 3-2 of only 32%. The effects of multiple variations from the system that gives the most consistent estimates (Figure 3-7) is summarized in Table 3.2.

3.8 Summary

Previous measurements have shown that motion measurements made with computer microvision are very repeatable. However, these results only address variability of the measurements and not accuracy. Small variability does not guarantee small errors; measurements can be consistently wrong.

To characterize accuracy, we have measured motion of non-overlapping analysis regions that span the width of the shuttle. We used computer microvision to measure the out-of-plane motion of each region. Under the assumption that the shuttle moves

as a rigid body, the real and imaginary components of the displacements in each region should be linear functions of distance across the shuttle.

Using the original system (Davis, 1994), measured motions differed from the best rigid motions by more than 30% of the measured motions (Figure 3-2). We identified four areas that caused errors: analysis regions with multiple moving structures (Sec. 3.2), nonuniform illumination (Sec. 3.3), contaminated background images (Sec. 3.4), and inferior optics (Sec. 3.5). We developed improved methods to reduce the effects of these sources of errors. The improved methods reduced deviations from rigid motions by more than a factor of 25.

Chapter 4

2-D Measurements

Two-dimensional measurements are easy to obtain with computer microvision. Images are acquired for only one plane of focus. They can then be analyzed to estimate in-plane motions of the gyroscope. 2-D analysis was used on the gyroscope to measure in-plane motions of the shuttles and to find the resonant frequencies of the gyroscope for the tuning fork (shuttles moving in opposite directions) and hula (shuttles moving in the same direction) modes of motion. Understanding these modes of motion is important in designing a good gyroscope. The gyroscope operates at the resonance of the tuning fork mode. However, the hula mode is unwanted and should be attenuated as much as possible at the operating frequency. This chapter investigates these in-plane modes of motion.

An example of results obtained from stimulating the gyroscope at resonance is shown in Figure 4-1. This shows the driven motion of the gyroscope shuttle, along with the motion in the in-plane orthogonal direction. Estimates such as these can be obtained very quickly using computer microvision. It takes 30 seconds to take the images and 2-4 seconds to analyze them. (Analysis time varies depending on the size of the images, the size of the region being analyzed, and the computer doing the analysis. I used a 100 MHz Pentium.) Obtaining background images for two point correction takes an extra 10 minutes, but it is only necessary to take these images once for each experiment configuration. Results such as these can be obtained at various frequencies or for various regions.

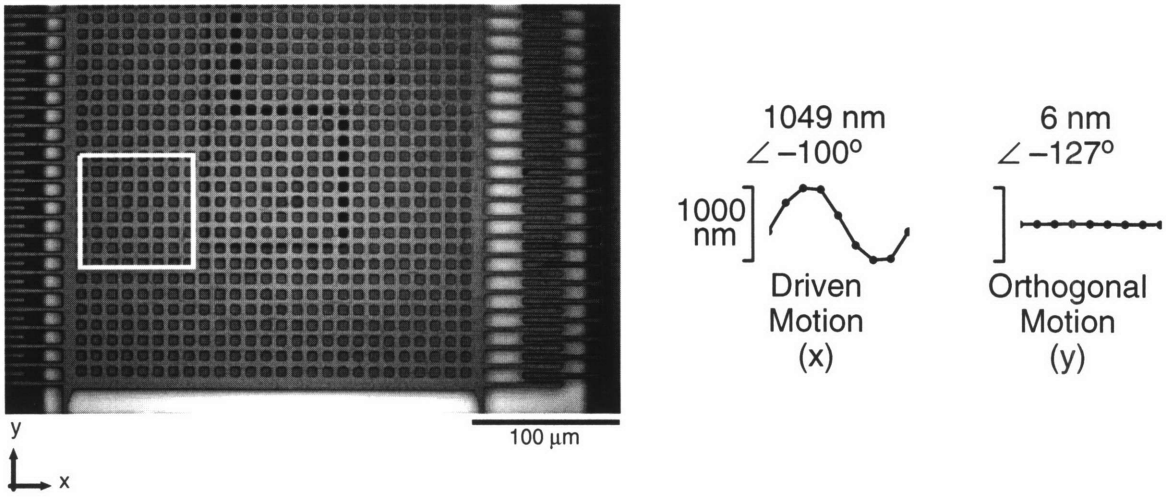

Figure 4-1: Motion of gyroscope shuttle at resonant frequency. The image shows one of the moving shuttles of the gyroscope, with the white box indicating the region that was analyzed. The gyroscope was driven by exciting the outer combs (see Figure 2-1, stimulus condition 1) with a 40 V peak-to-peak AC + 20 V DC stimulus at 18.9 kHz. The plots show the estimated displacement for both the driven motion and the motion in the orthogonal direction. Magnitude and phase are indicated.

4.1 Frequency response of Tuning Fork Motion

To obtain a frequency response of the motion of the shuttle, the region shown in Figure 4-1 was analyzed using stimulus frequencies between 500 Hz and 23 kHz. Figure 4-2 shows the resulting magnitude and phase of the driven motion plotted versus frequency. Data for each frequency was taken five times, and the plots show the mean and standard deviation of the results at each frequency. These results demonstrate the large dynamic range and low noise floor of the computer microvision system. Motions spanning two orders of magnitude were measured. The standard deviation of repeated trials is over an order of magnitude below the mean magnitude and less than five degrees in phase. The resonant frequency of 18.9 kHz agrees with both previous information (Mark Weinberg, personal communication) and visual observations. The results show that the system has a Q of about 100 (in air).

Each image requires 3.75 seconds to acquire. This time is limited by the amount of time needed to get sufficient light from the LED. Eight images are needed for each

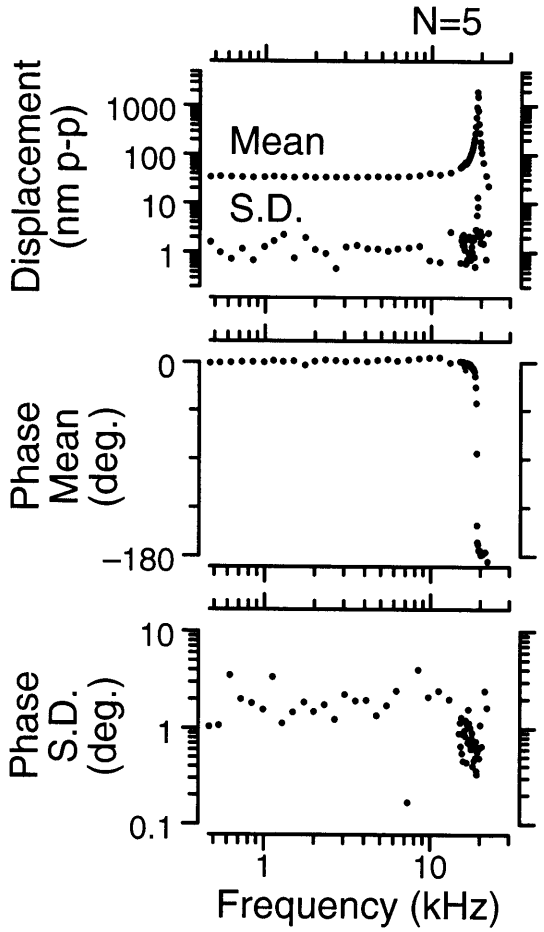

Figure 4-2: Frequency response of the gyroscope when the outer comb drives are excited with a 40 V peak-to-peak AC + 20 V DC stimulus (stimulus condition 1, Figure 2-1). The region shown in Figure 4-1 was analyzed at 60 different frequencies. Each experiment was performed 5 times. The plots show the mean and unbiased standard deviation of the magnitude and phase of the fundamental of the driven motion as a function of the input frequency. The peak is at 18.9 kHz. The Q is 108. The gray phase point is at the resonant frequency of the hula mode of motion.

frequency point, requiring 30 seconds per point. Each image is 576 $\times$ 382 pixels with 12 bits per pixel, which requires 325 kbytes of disk space per image (2.5 Mbytes per point). Thus, data acquisition time for each frequency response used in Figure 4-2 was 30 minutes (30 seconds per point for 60 points). Analysis time on a Pentium 100 was 3 minutes. The results for the five repetitions shown were acquired in 2.5 hours and analyzed in 15 minutes. They required 760 Mbytes of disk space.

4.2 Frequency response for "Hula" Motion

The frequency dependence of the "hula" mode of motion was investigated by exciting the gyroscope using a different electrode configuration (stimulus condition 2, Figure 2-1). Results show two peaks, as seen in Figure 4-3. The gyroscope was visually observed at both these frequencies to correlate the mode of motion with the excitation frequency. The first peak corresponds to the "hula" motion, and the second peak corresponds to the tuning fork motion.

Knowing the resonance of the hula mode can help us understand Figure 4-2 better. The hula resonance appears in this figure even though the gyroscope was driven to reject hula motion. This can be seen clearly in the phase plot, where there is a gray point below the curve of the phase. This point is at the hula mode's resonance.

4.3 Discussion

The speed of motion measurements for 2-D analysis is primarily determined by the integration time needed for the LED. These results show that motion estimates can be obtained in a couple of minutes. A frequency analysis can be done in about a half an hour (depending on the number of frequency points required). This is too slow for real-time estimates, but it is comparable to the time required to obtain some electrical measurements using a spectrum analyzer. The time required for 2-D analysis is much less than that required for 3-D analysis, which will be demonstrated in Chapter 5. Two-dimensional analysis also requires an order of magnitude less disk space than is

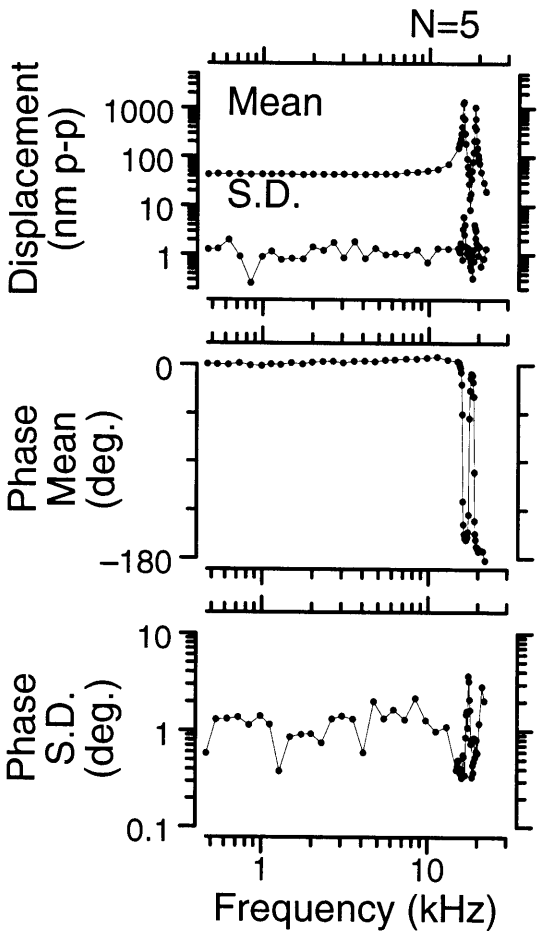

Figure 4-3: Frequency response of the gyroscope when only one comb drive is excited (stimulus condition 2). These plots were created as described in Figure 4-2. The first peak (16.1 kHz) corresponds to the hula mode resonance, and the second peak (18.9 kHz) is the tuning fork mode resonant frequency.

required for 3-D analysis, which typically requires 30 times as much disk space. The speed and disk space requirements make 2-D analysis advantageous over 3-D analysis when measuring in-plane motions.

Two-dimensional analysis demonstrates that computer microvision is very precise. The standard deviations measured could be due to variation in the gyroscope or noise in the measurements. The low deviations indicate that the gyroscope's motion is repeatable and that computer microvision is very precise.

Two-dimensional frequency analysis can reveal spectral modes of motion which correspond to different mechanical modes of the gyroscope. Novel stimulus conditions were used to excite two different mechanical modes of motion: hula mode and tuning fork mode. Understanding unwanted modes of motion can help eliminate these modes. For example, understanding the hula mode helped designers ensure that there was frequency separation between the two modes. This was important because even when the gyroscope is stimulated to reject the hula motion, the mode is excited at its resonance, as is demonstrated in Figure 4-2 by the gray point at the hula mode resonant frequency. Thus, 2-D analysis can give insights into mechanical modes of motion.

Chapter 5

3-D Measurements

As explained in Chapter 1, out-of-plane motions of the gyroscope are of particular interest because they are interpreted as angular velocity. Computer microvision is a useful method for measuring these out-of-plane motions because it can estimate three-dimensional motions for all the structures in an image simultaneously. While other measurement systems can measure out-of-plane motions, they typically cannot also measure in-plane and out-of-plane motions simultaneously. Laser Doppler systems, for example, can measure only one point at a time, and only give estimates in one direction. By measuring 3-D motions, we can compare in-plane and out-of-plane motions. Measuring different regions of the shuttle allows us to characterize mechanical modes of motion. These 3-D measurements help us understand out-of-plane modes of motion that may limit the sensitivity of the gyroscope.

To measure 3-D motions, 3-D data sets are used. An example of a 3-D data set is shown in Figure 5-1. This region of the shuttle was analyzed at resonance to find the 3-D motions of the shuttle (Figure 5-2). The measurements were repeated five times to find the mean and standard deviation. Notice the large dynamic range of the computer microvision system, which simultaneously measured orthogonal motions that differed by more than two orders of magnitude. The measurements are also very repeatable — 5 nm for in-plane motions and 13 nm for out-of-plane motions. (We expect out-of-plane motions to be less precise because the optics of the microscope have worse resolution along the out-of-plane axis.) The out-of-plane motions are not

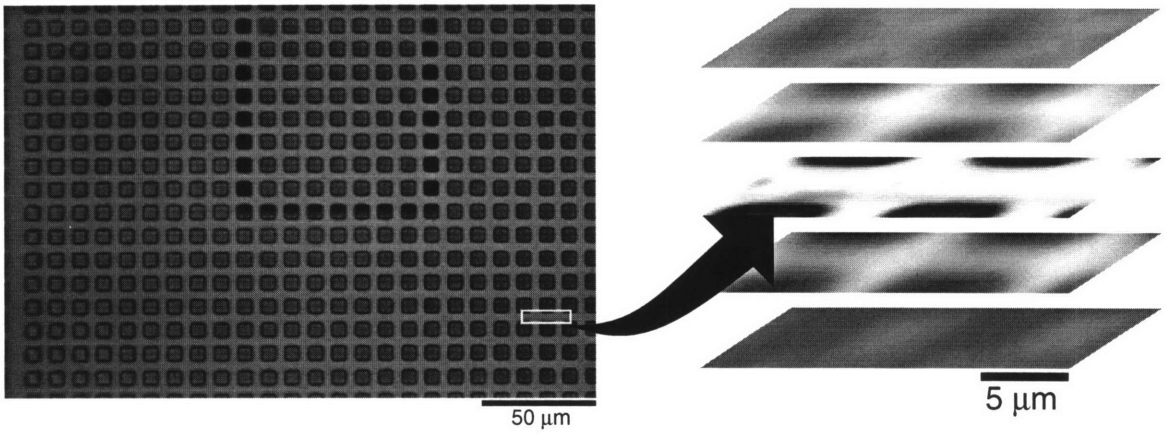

Figure 5-1: The left panel shows the analysis region of the shuttle. The right panel shows this same region enlarged, contrast-enhanced, and projected with perspective, along with planes above and below the in-focus plane, illustrating how a 3-D image is formed. The planes shown are separated by 3.8 μm.

in phase with the in-plane motions.

A disadvantage to these 3-D measurements is they require more time. Obtaining the data for this example took 24 minutes, not including the time it took to get the background images (which is an additional 10 minutes). Analyzing the data takes about one minute on a Pentium 100 system.

5.1 Frequency response of out-of-plane motions

The analysis shown in Figure 5-2 was performed at frequencies ranging from 500 Hz to 50 kHz to obtain a frequency response of both the in-plane and out-of-plane motion of one region of the gyroscope shuttle (Figure 5-3). Both in-plane and out-of-plane motions are resonant, and the resonant frequencies are different. The in-plane resonance is at 18.9 kHz, and the out-of-plane resonance is at 24.4 kHz. The out-of-plane motion is also much more damped. One would expect both resonances to be much sharper in a vacuum. The out-of-plane motion is more damped in air due to squeeze-film damping (Weinberg et al., 1994). Notice the spurious phase point (plotted in gray) in the in-plane response and the lower than expected magnitude

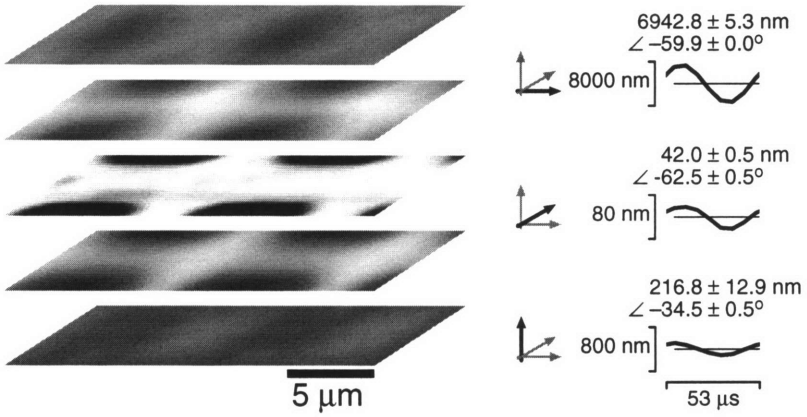

Figure 5-2: Out-of-plane motions of the shuttle. Thirty planes (5 of which are shown) spanning 16 μm were imaged at 8 evenly-spaced phases of an 18.9 kHz stimulus (40 V AC peak-to-peak + 20 V DC). The tuning fork stimulus condition (stimulus condition 1, Figure 2-1) was used. The experiment was repeated 5 times, and mean and standard deviation of the fundamental motion are shown, along with the time waveforms for each component of the motion. Note the vertical scale change in each plot.

point (gray) at that same frequency. This frequency is the resonant frequency of the hula mode of motion. Also note that there appear to be three sub-peaks in the out-of-plane motion. The first corresponds to the resonant frequency of the in-plane motion. The other two will be explained later. Image acquisition took 20 hours and data analysis took 15 minutes.

5.2 Out-of-plane modes of motion

We have examined the out-of-plane motion of one region of the shuttle at several frequencies. However, we would also like to know how the out-of-plane motion differs for different regions of the shuttle. Information about *how* the shuttle is moving out-of-plane could lead to ideas about how to prevent these out-of-plane motions.

To analyze spatial modes of motion, 12 regions across the shuttle were analyzed (Figure 5-4). Two stimulus conditions were analyzed at a frequency off resonance so that larger stimuli could be used and more out-of-plane motion would be induced.

Figure 5-5 shows the in-plane and out-of-plane motion when the gyroscope is

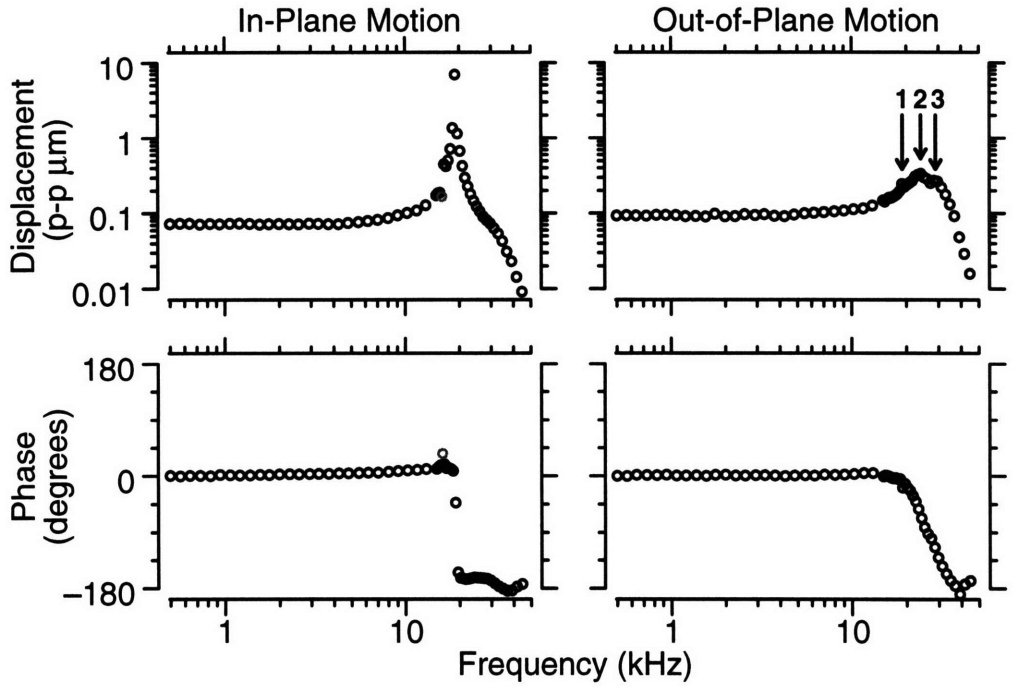

Figure 5-3: Frequency response of a Draper gyroscope. The experiment described in Figure 5-2 was repeated at several different frequencies. The magnitude and phase of the fundamentals of the in-plane (driven) and out-of-plane motion are shown as a function of the stimulus frequency. The gray points on the in-plane motion response are at the resonant frequency of the hula mode of motion. The arrows indicate 3 sub-peaks in the out-of-plane response that can be correlated with 3 modes of motion.

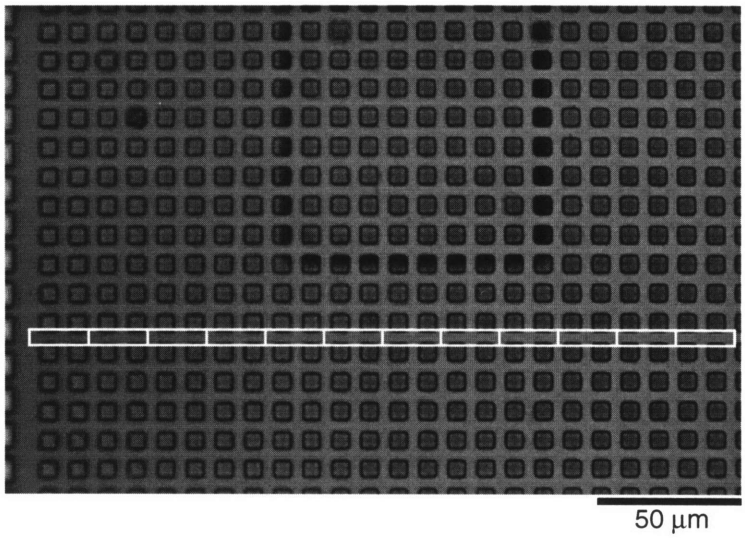

Figure 5-4: Twelve regions (white rectangles) used to analyze out-of-plane modes of motion.

driven in tuning fork mode (stimulus condition 1, Figure 2-1). The in-plane motions are similar for all 12 regions; however, the out-of-plane motions show that one side of the shuttle moves more than the other. This out-of-plane motion is mostly levitation, with a small amount of rocking. Figure 5-6 is a graphical representation of the data. It shows the in-plane and out-of-plane displacements of each of the 12 regions for the 8 phases of motion. The motions have been exaggerated for clarity.

A different stimulus condition (stimulus condition 3, Figure 2-1) was used to excite the rocking mode of motion. The results shown in Figure 5-7 were obtained when the inner comb of the shuttle was excited. Note that one edge of the shuttle is 180 degrees out of phase with the other edge, and the sections near the middle are hardly moving. This motion describes a rocking motion with a pivot point near the center of the shuttle. The rocking motion can be seen more clearly in Figure 5-8.

The analysis was also performed at resonance (18.9 kHz) using stimulus condition 1 to estimate the out-of-plane motions at resonance. This is the stimulus condition normally used to operate the gyroscope. Results are shown in Figure 5-9 and Figure 5-10. The electrical stimulus used was half that used in the previous two experiments because the gyroscope has large in-plane motions at resonance. Again we observe a levitation mode of motion with some rocking.

We can measure modes of motion from a single set of data. The time to take the data for these experiments was 24 minutes. The analysis took 5 - 15 minutes.

5.3 Modal Decomposition

The out-of-plane motion observed using stimulus condition 1 is a combination of rotation and levitation. This motion can be decomposed into the portion due to rotation (rocking mode), and the portion due to levitation as follows

$$z(x,t) = L(t) + x \tan A(t) \tag{5.1}$$

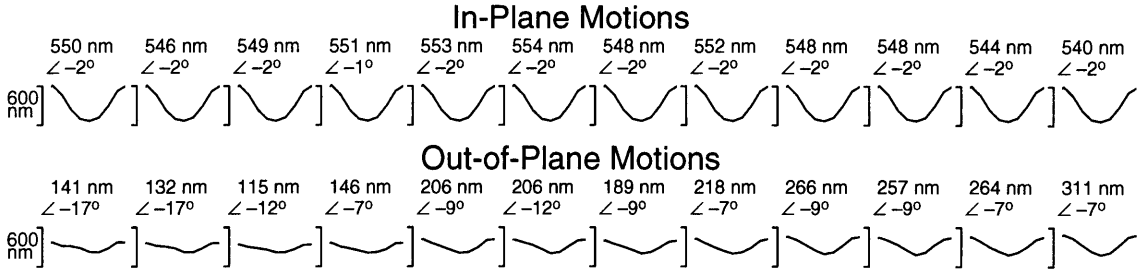

Figure 5-5: In-plane and out-of-plane estimates of motion. The top plots show the in-plane motion and the bottom plots show the out-of-plane motion for each of the 12 regions shown in Figure 5-4. The order of the plots corresponds to that of the regions. An 80 V peak-to-peak AC + 40 V DC stimulus at 13 kHz was used to excite the gyroscope using the first stimulus condition (Figure 2-1).

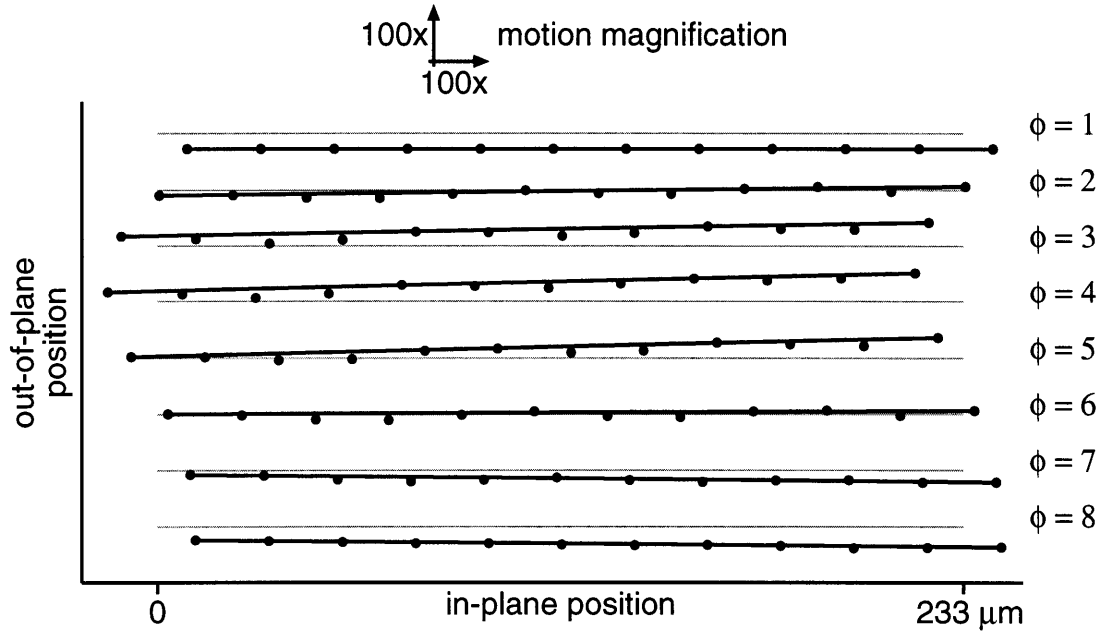

Figure 5-6: In-plane and out-of-plane motions of the shuttle. The estimated in-plane and out-of-plane positions of each region are represented by the dots. The displacement for each of 8 phases (one period of the motion) is shown as separate lines. The motions are magnified by 100 relative to the length of the shuttle for clarity. The gray lines give a stationary reference position of the shuttle for each phase. These results are for stimulus condition 1, with a stimulus of 80 V peak-to-peak AC + 40 V DC at 13 kHz.

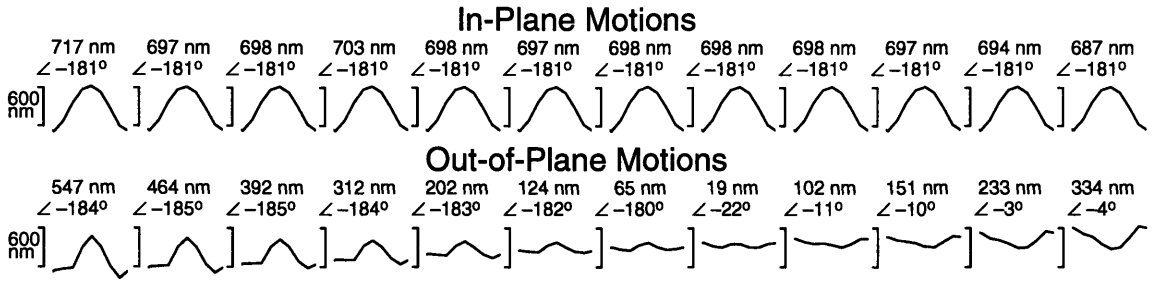

Figure 5-7: In-plane and out-of-plane estimates of motion when the inner comb of the shuttle is excited with a 13 kHz stimulus. Other aspects of the figure are as described for Figure 5-5.

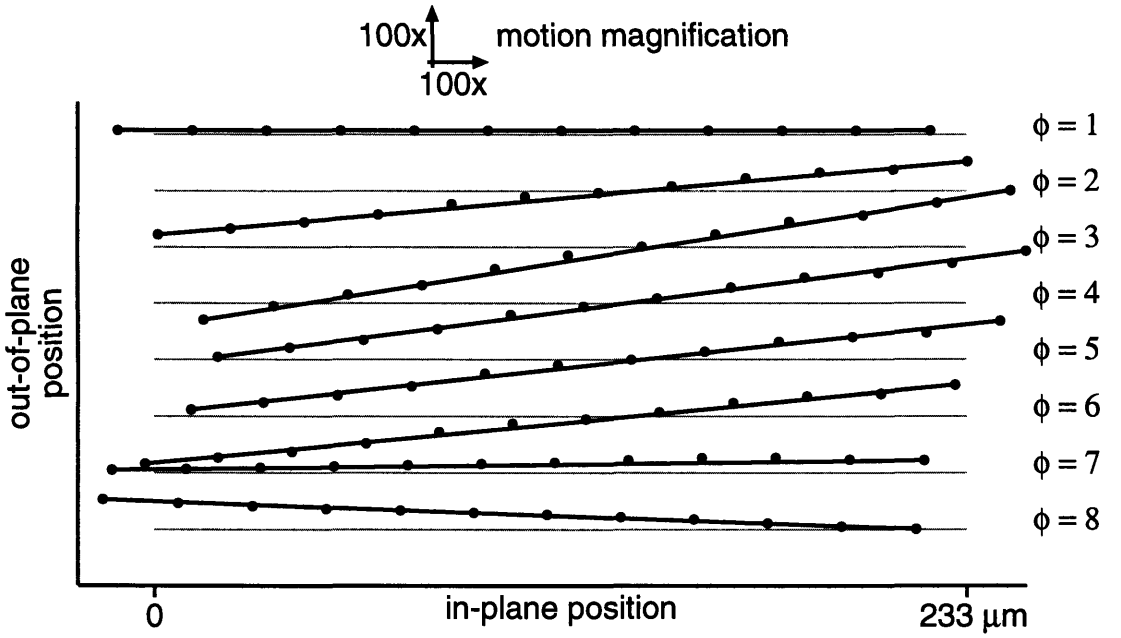

Figure 5-8: In-plane and out-of-plane motions. Stimulus condition 3 (inner comb excited) was used with a 13 kHz stimulus to obtain this data. Other aspects of the figure are as described for Figure 5-6.

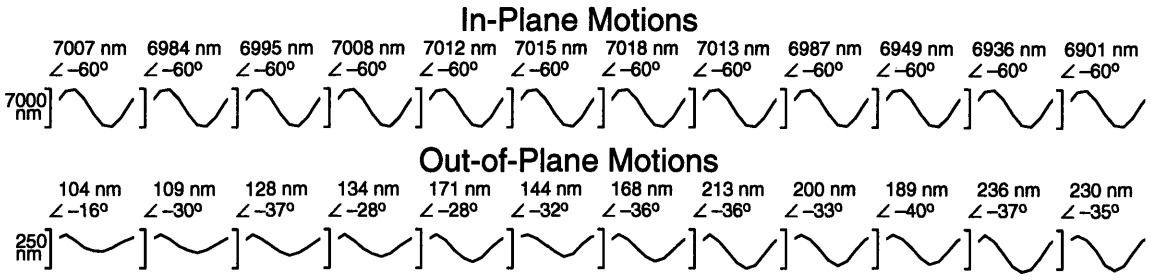

Figure 5-9: In-plane and out-of-plane estimates of motion. For these plots, a 40 V peak-to-peak AC + 20 V DC stimulus at a frequency of 18.9 kHz was used. The first stimulus condition (outer combs excited) was used. Note that the scales are different between the two plots. Other aspects of the figure are as described for Figure 5-5.

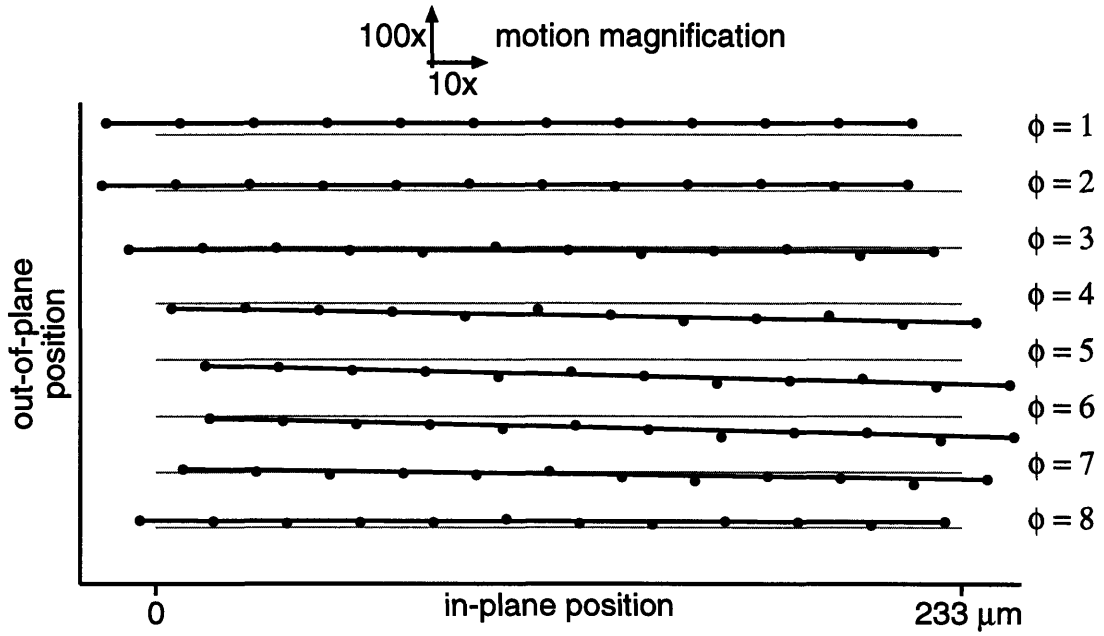

Figure 5-10: In-plane and out-of-plane motions. This data was obtained at resonance (18.9 kHz) for a 40 V peak-to-peak AC + 20 V DC stimulus. The outer combs of the gyro were excited, as in stimulus condition 1 (Figure 2-1). Other aspects of the figure are as described for Figure 5-6.

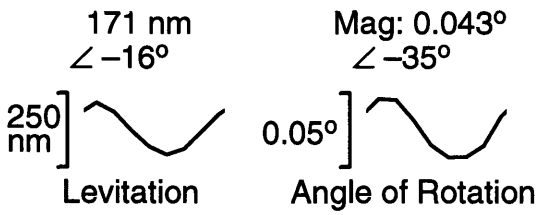

Figure 5-11: Levitation and rotation waveforms for out-of-plane motion at resonance. The data shown in Figure 5-9 was decomposed into levitation and rocking motion. The plot on the left shows the motion due to levitation for each of the regions across the shuttle. The plot on the right shows the angle of rotation as a function of time. Levitation is measured as the average motion at the center of the gyroscope.

where $L(t)$ represents the out-of-plane levitation as a function of time, x represents the distance from the center of the shuttle, and $A(t)$ represents the angle between the shuttle and substrate as a function of time. From out-of-plane motion estimates and the position of each region along the shuttle, we can use Eq 5.1 to estimate levitation and rocking. The best-fitting line through the estimates was determined for each phase of the motion. The arctangents of the slopes for each phase were plotted vs. phase to obtain the angle of rotation waveform shown in Figure 5-11. Levitation was determined from the center points of the best-fitting lines. Figure 5-11 shows the waveforms for the levitation and angle of the motion at resonance. Notice that the phases of the two modes are different.

5.4 Frequency Response of Modes

By analyzing the 12 regions shown in Figure 5-4 at different frequencies, we can obtain a frequency response of the rocking and levitation modes of motion. The response of the levitation mode of motion is shown in Figure 5-12. Figure 5-13 shows the response for the rocking mode of motion. These two modes of motion explain the last two sub-peaks in the out-of-plane motion frequency response (Figure 5-3). The tallest peak is the levitation mode of motion, and the last peak is the rocking mode of motion. The spurious phase point (gray) in the rocking mode frequency response (Figure 5-13) and the magnitude point that looks too high (gray) in the levitation

mode frequency response are at the in-plane resonant frequency. (There is also a noticeable break in both responses at 20 kHz, which is where the filter was changed from the 22 kHz cut-off filter to the 48 kHz cut-off filter.) These modal frequency responses took 1 hour and 40 minutes to analyze.

5.5 Discussion

While obtaining 3-D data takes much longer than obtaining 2-D data, a lot more information can be obtained from one data set. The in-plane, out-of-plane, and modal frequency response shown in this chapter were all obtained from one data set. Also, all these responses can be obtained from the same analysis; the results are just presented in different ways.

These results show that by combining 3-D motion estimates from different regions, computer microvision can be used to characterize complex modes of motion that had not been measured previously. Computer microvision successfully identified two out-of-plane modes of motion and found where they were excited. When the gyroscope was being designed, the designers became aware of the hula mode of motion and carefully adjusted the design so it would not be excited at the same frequency as the tuning fork mode of motion. We expect that knowledge of these out-of-plane modes of motion will similarly be useful in improving the design of the gyroscope.

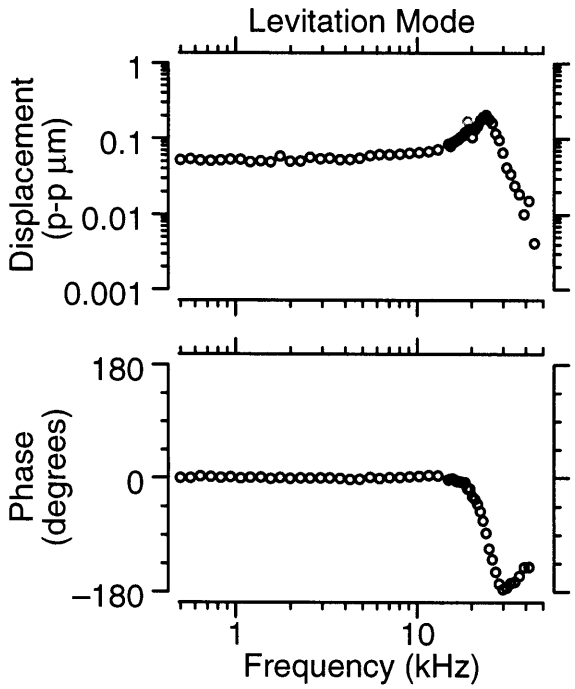

Figure 5-12: Frequency response of levitation mode of motion. Regions along the length of the shuttle were analyzed to determine the average motion not accounted for by rotation. A pivot point in the center of the shuttle was assumed. The magnitude and phase of the levitation for frequencies between 500 Hz and 50 kHz are shown. A resonant frequency of 24 kHz is visible. The stimulus was 40 V peak-to-peak AC + 20 V DC in stimulus condition 1 (Figure 2-1). The gray magnitude point is at the in-plane resonance.

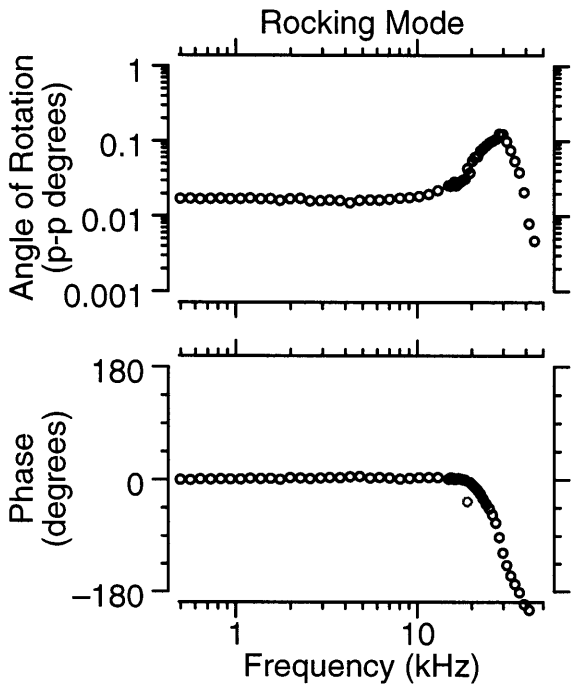

Figure 5-13: Frequency response of rocking mode of motion. Motions of 12 regions along the length of the shuttle were used to create the angle waveform between the shuttle and the substrate. The angle as a function of time was found using the arctangent of the slope of the best-fitting line through the shuttle displacements (i.e., finding the angle between each gray and black line in Figure 5-10). The magnitude and phase of the fundamental component of this waveform for frequencies between 500 Hz and 50 kHz are shown. The resonance of the rocking mode is at 29 kHz. The stimulus was 40 V peak-to-peak AC + 20 V DC in stimulus condition 1 (Figure 2-1). The gray phase point is at the in-plane resonance.

Chapter 6

Discussion

6.1 Significance of results to computer microvision

The analysis of the gyroscope has improved computer microvision by making it more robust. As shown in Chapter 3, initially there were several problems that plagued the results. Because we had a priori knowledge of what motion was feasible and what was not, we were able to correct these problems. A better light source was identified, a new method was developed for taking background images, and the significance of parameters such as numerical aperture of the objective and effect of analysis region was investigated. The issues affecting performance are not completely understood and will need further investigation. However, the performance of computer microvision was improved to the point that interesting results could be obtained for the gyroscope.

6.2 Significance of results to gyroscope design

Two-dimensional analysis allowed us to characterize known modes of in-plane motion that were important in the design of the gyroscope. Using three-dimensional analysis, out-of-plane modes of motion that had not previously been measured were characterized. These modes are important to understand because the gyroscope uses out-of-plane motions to determine its angular velocity. We expect characterization of these modes can be used to improve future gyroscope designs. For example, it

may be possible to better separate the in-plane and out-of-plane resonances so that out-of-plane motions in the absence of rotation are attenuated.

The measurements of the levitation and rocking modes of motion are the first to be done on the gyroscope. The next step is to identify the cause of these modes so that they can be controlled. Computer microvision may also be useful here. For example, the hula mode of motion is mostly rejected in the gyroscope's normal operating mode (stimulus condition 1, Figure 2-1). However, by using another stimulus condition (stimulus condition 2), we were able to excite this mode of motion. Similarly, by using a different stimulus condition (stimulus condition 3), we were able to excite a predominantly rocking mode of motion (Figure 5-7 and Figure 5-8). This additional knowledge may help pinpoint the cause of the rocking mode of motion.

6.3 Significance of computer microvision to MEMS

The analysis of the gyroscope shows that computer microvision can be used to obtain useful results for a microelectromechanical system. Computer microvision does require a lot of time to obtain 3-D data. However, the resulting measurements are very comprehensive. 3-D estimates allow complete characterization of the motion, unlike scalar measurements where other components of the motion may confound the estimates. Furthermore, motions of all identifiable structures in the images can be measured, which allows characterization of modes of motion. Computer microvision is also a very precise measurement tool with noise floors on the order of 5-10 nanometers. Computer microvision is also useful for MEMS because of its large dynamic range of (1) magnitudes of motions it can measure, (2) frequencies it can span, and (3) sizes of regions it can analyze. As robustness and quality of computer microvision increase, we expect computer microvision to become a useful tool for MEMS designers.

Bibliography

Aranyosi, A. J. (1997). Derived probability distribution for a ratio of poisson variables. Internal Memo, Massachusetts Institute of Technology, Cambridge, MA.

Bernstein, J., Cho, S., King, A. T., Kourepenis, A., Maciel, P., and Weinberg, M. (1993). A micromachined comb-drive tuning fork rate gyroscope. In *Technical Disgest of the Solid-State Sensor and Actuator Workshop*, pages 143–148, Hilton Head Island, SC. Transducers Research Foundation, Inc.

Davis, C. Q. (1994). Estimation of sub-micrometer translations of a rigid body using light microscopy. Master's thesis, Massachusetts Institute of Technology, Cambridge, MA.

Davis, C. Q. (1997). Measuring nanometer, three-dimensional motions with light microscopy. PhD thesis, Massachusetts Institute of Technology, Cambridge, MA.

Davis, C. Q. and Freeman, D. M. (1997). Using video microscopy to measure 3d cochlear motions with nanometer precision. In *Abstracts of the Twentieth Midwinter Research Meeting*, St. Petersburg Beach, Florida. Association for Research in Otolaryngology.

Freeman, D. M. and Davis, C. Q. (1996). Using video microscopy to characterize micromechanics of biological and manmade micromachines. In *Technical Disgest of the Solid-State Sensor and Actuator Workshop*, pages 161–167, Hilton Head Island, SC. Transducers Research Foundation, Inc.

Hiraoka, Y., Sedat, J. W., and Agard, D. A. (1987). The use of a charge-coupled device for quantitative optical microscopy of biological structures. *Science*, 238:36–41.

Horn, B. K. and Schunck, B. G. (1981). Determining optical flow. *Artificial Intelligence*, 17:185–203.

Horn, B. K. P. and Weldon, Jr., E. (1988). Direct methods for recovering motion. *Internatl. J. of Computer Vision*, 2:51–76.

Horowitz, P. and Hill, W. (1991). *The Art of Electronics.* Cambridge University Press, Cambridge, MA.

Inoué, S. (1986). *Video Microscopy.* Plenum Press, New York, NY.

Kleppner, D. and Kolenkow, R. J. (1973). *An Introduction to Mechanics.* McGraw-Hill Inc., New York.

O'Connor, L. (1992). Mems: Microelectromechanical systems. *Mechanical Engineering*, 114(2):40–47.

Weinberg, M., Bernstein, J., Cho, S., King, A. T., Kourepenis, A., and P., W. (1994). Micromechanical tuning fork gyroscope test results. In *Proceeding of the AIAA GN&C Conference*, Scottsdale, AZ.

Young, I., Zagers, R., van Vilet, L., Mullikin, J., Boddeke, F., and Netten, H. (1993). Depth-of-focus in microscopy. In *Proceedings of the 8th Scandinavian Conference on Image Analysis*, pages 493–498, Tromsoe, Norway. Scandinavian Conference on Image Analysis.